

Unsteady Heat Flux Measurements of Junction Flow With Reynolds Number and Freestream Turbulence Effects

Syed S. Elahi ¹, Zachary K. Moul ², Eric A. Lange ³ and Stephen P. Lynch ⁴
The Pennsylvania State University, State College, PA, 16802

Turbulent junction flow is a three-dimensional unsteady phenomenon occurring in the flow upstream of the leading edge of bodies attached to a surface, such as in turbine rotors and stators, heat exchangers, submarine appendages, and wing-fuselage attachments. One of the signature features of this type of flow is the presence of bimodal behavior in the probability density functions of velocity, but the bimodal phenomenon has not been observed in surface heat flux measurements. However, it is well-known that time-mean levels of heat flux are significant. In situations where the body experiences high freestream turbulence, mean heat flux is further increased, but the mechanisms of the enhancement are unclear. In this paper, a test section for simultaneous time-resolved heat flux and flowfield measurements in front of a common research wing is highlighted. Time-resolved unsteady heat flux is also reported for a range of Reynolds numbers at high freestream turbulence. Time-resolved heat flux measurements from the symmetry plane of the junction region are compared with measurements downstream of the airfoil to determine if there are correlated behaviors. Also, a comparison between the effects of baseline freestream turbulence and high freestream turbulence on junction heat transfer is presented. It is found that at the plane of symmetry, high freestream turbulence increases endwall heat transfer at low Reynolds number and has negligible influence on endwall heat transfer at high Reynolds number.

Key words: Junction flow, Reynolds number, Turbulence, Unsteady heat flux

Nomenclature

G	=	Auto spectral density function	Sk	=	Skewness
C	=	Chord length	St	=	Stanton number
DAQ	=	Data acquisition system	St _{RMS}	=	Stanton number RMS
U _{ref}	=	Freestream velocity	St _{mean}	=	Stanton number time-averaged
T _∞	=	Freestream temperature	SPIV	=	Stereo particle image velocimetry
HS	=	Horseshoe	T _s	=	Surface temperature
q''	=	Heat flux [W/m ²]	ΔT	=	Temperature difference (T _s -T _∞)
I	=	Integral length scale	t	=	Time
Ku	=	Kurtosis	Tu	=	Turbulence intensity
LDV	=	Laser doppler velocimetry	Greek		
T	=	Maximum thickness of Rood wing	δ	=	Boundary layer thickness
PDF	=	Probability density function	δ*	=	Displacement thickness
PSD	=	Power spectrum density	ν	=	Kinematic viscosity at T=300K
PVC	=	Polyvinyl chloride	θ	=	Momentum thickness
RTS	=	Resistance temperature sensing element			
Re _r	=	Reynolds number based on max body thickness			
Re _θ	=	Reynolds number based on momentum thickness			

¹ Graduate research assistant, Mechanical and Nuclear Engineering.

² Undergraduate research assistant, Mechanical and Nuclear Engineering.

³ Graduate research assistant, Mechanical and Nuclear Engineering.

⁴ Assistant professor, Mechanical and Nuclear Engineering, AIAA Senior Member.

I. Introduction

TURBULENT junction flow, also known as the horseshoe (HS) vortex system, is formed when a two-dimensional boundary layer encounters a bluff body, which then separates from the wall to form a coherent vorticity. The unsteady behavior of the junction flow is responsible for significant pressure fluctuations and high heat transfer near the leading edge of the bluff body. Praisner and Smith [1] reported up to 300% increase in heat transfer in the junction flow region when compared with the upstream turbulent boundary layer. This rise in surface heat transfer can cause severe degradation in hot-section turbomachinery components such as turbine rotors and stators. Han et al. [2] stated that a change of component temperature by 25°C in the incoming flow within the hot-section turbomachinery (where nominal temperature is 1800°C) can reduce the part life by almost half. Devenport and Simpson [3] presented a detailed study of the junction flow for a single Reynolds number, which is representative of turbomachinery conditions. According to their study, the probability density functions of velocity demonstrates a bimodal peak [3], which represents two preferred states for the junction flow. Measurements by Praisner and Smith [1] at a lower Reynolds number also indicated bimodal behavior in the flowfield, and its impact on the steady heat flux. Lewis et al. [4] presented probability density functions of wall heat flux measurements in the region near the observed bimodal velocity fluctuations, which surprisingly did not show the bimodal behavior. However, it is unknown whether this a function of Reynolds number, and what impact freestream turbulence might have (as is typical in turbomachines). In this paper, an experimental setup is presented that captures time-resolved unsteady heat flux measurements over a range of Reynolds numbers as well as a baseline low freestream turbulence and high freestream turbulence level. Also, time-resolved endwall heat transfer from the symmetry plane is compared with places around the wing body to investigate any coupling effects due to turbulence and/or Reynolds number.

II. Previous Studies

The turbulent junction flow or horseshoe (HS) vortex system is a three-dimensional vortical structure commonly found in aircraft wing roots, fin-tube interfaces in heat exchangers, submarine hulls/appendages, and in junctions of turbomachinery components such as rotors and stators. An adverse pressure gradient is formed by an obstacle [3] which causes the approach boundary layer to separate. A primary vortex, as well as secondary and tertiary vortices are formed, and follow the outline of the obstacle before merging with vortices generated by the trailing edge [5]. Several previous studies have described the causes of high turbulence intensities, pressure fluctuations, and endwall heat transfer within the HS vortex region ([1],[3]). Devenport and Simpson reported the unsteadiness in the incoming large-scale eddies contributed to the high turbulence intensities in the vortex core [3].

One of the signature features of a horseshoe vortex is the presence of two quasi-steady modes in the PDFs of streamwise velocity components ([3],[5]). The coherent upstream mode is called “backflow mode” and a more chaotic mode near the leading edge is called “zero-flow mode”[3]. Anderson and Lynch [6] also showed the presence of these two quasi-steady modes in their measurements of the HS vortex in front of a circular pin in a fully developed channel flow. Numerical simulations by Paik et al. [7] and Yakhov et al. [8] further supported the existence of quasi-steady modes in the vortex behavior in front of bluff bodies. Recent studies by Apsilidis et al. [9] and Chen et al. [10] on junction flow using cylindrical bodies demonstrated a third mode called “intermediate mode” which persists between the backflow mode and zero-flow mode.

Praisner and Smith [1] and Hada et al. [11] complemented time mean flowfield measurements with time mean heat transfer measurements to help explain the convective heat transfer at the junction. They found a primary high heat transfer band very close to the junction, which follows the leading edge contour, and a further upstream secondary high heat transfer band linked to the secondary vortex upstream of the large primary vortex. Hada et al. [11] also examined the effects of varying boundary layer thickness, body thickness of the bluff body, and incoming Reynolds number on the surface Stanton number and found that the double bands of high wall heat transfer persisted in all those instances. Swisher et al. [14] investigated the unsteadiness in heat flux along the stagnation streamline in front of a streamlined cylinder using a high-frequency-response heat flux microsensors (HFM) and found an increase in the RMS of heat flux unsteadiness as much as 30% over the mean heat flux in the vortex core. However, there has not been much research in exploring the spatially and time-resolved heat flux over a range of Reynolds numbers (Re) and turbulence intensities (Tu). For example, Lewis et al. [4] examined the spatially and time-resolved heat flux, but their results were limited to single Re and Tu .

Several efforts were made previously to understand the contributions of high freestream Tu and Re on time-averaged endwall heat transfer in gas turbine vanes ([15],[16]). Blair [12] and Dunn et al. [13] were among the initial researchers who investigated the endwall heat flux rates between turbine cascade blades and reported an increase by a factor of 3 near the leading edge of endwall and turbine junction. Radomsky and Thole [15] introduced

a freestream turbulence of 20% and found a 15% increase in endwall heat transfer underneath the horseshoe vortex core. Kang et al. [16] reported that secondary flows contributed to the increase of the trailing edge endwall heat transfer of a vane. Ames et al. [17] furthered the research efforts of understanding vane endwall heat transfer by introducing a mock aeroderivative combustion system upstream of a turbine vane cascade, where turbulence levels ranged from 0.7% to 14% and inlet Reynolds numbers based on true chord length and exit conditions were as high as 2,000,000. Ames et al. [17] reported that while secondary flows (including the leading edge junction flow) had noticeable impact on surface heat transfer at low turbulence levels, they had negligible impact at higher turbulence levels, especially for high Reynolds numbers.

Only a limited number of studies have provided both mean and RMS of heat transfer, and of those studies, there has been no investigation over a range of Reynolds number and freestream turbulence levels. Thus, the effects of those two parameters on the convective heat transfer in a junction flow is not well-understood. This paper investigates the effect of high freestream turbulence on junction region heat transfer over a range of Reynolds numbers. A particular interest here is examining the temporally resolved nature of the junction heat transfer, which may be linked to the bimodal nature of the junction flow and could be sensitive to freestream turbulence effects.

III. Experimental Setup

A. The Facility

A large recirculating low speed wind tunnel is used to conduct all experiments for this paper. As highlighted in Figure 1, a fan is used to circulate air around the wind tunnel and different stages of pre-conditioning to the flow are applied via heat exchangers to maintain the freestream air temperature at the desired levels. Also shown in Figure 1 is a test section with sufficient optical accessibility for flow and surface heat transfer diagnostics. Polycarbonate is used for constructing the sidewalls as well as the top wall. Also, sections from the side and top walls have glass for better optical accessibility. For the current studies, freestream turbulence is generated via a grid system of parallel vertical cylinders, which is positioned 14.6 grid bar diameters upstream of a modified NACA 0020 airfoil, also known as Rood wing (3:2 semi-elliptical airfoil leading edge and NACA 0020 trailing edge connected at the

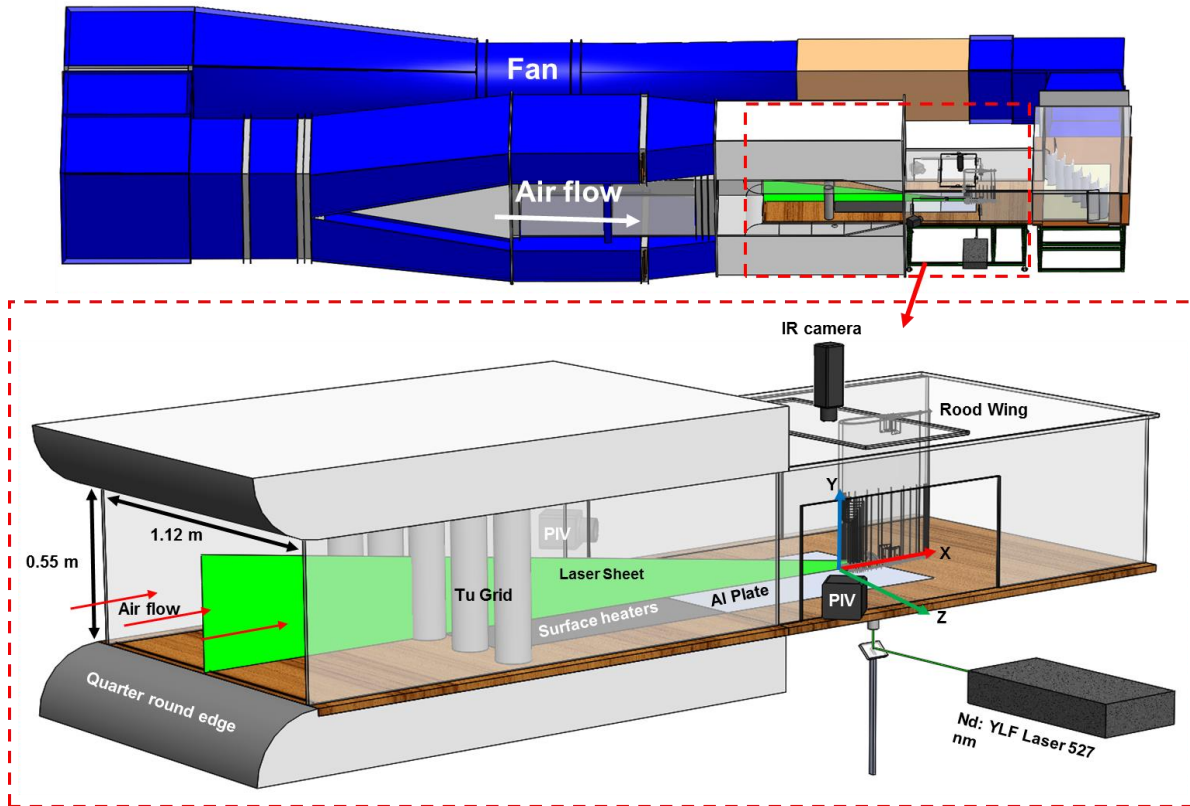


Figure 1. A recirculating low speed wind tunnel is presented with high speed flowfield measurement capabilities as well as endwall heat transfer measurement tools.

maximum thickness) [3]. The width and height of the test section around the airfoil are 1.12m and 0.55m respectively.

Also shown in Figure 1, the streamwise direction is chosen as the positive x-direction, y-direction is chosen to be the normal to the endwall, and right hand rule is applied to designate the z-direction. The origin of the coordinates is position at the leading edge of the Rood wing. The single airfoil shown in Figure 1 has a 0° angle of attack with a symmetry along the centerline. The dimensions of this airfoil are a chord (C) of 40 cm, a span (S) of 54.50 cm, and a maximum thickness (T) of 9.42 cm. This airfoil is hollow in the middle and is made out of stereolithographic process. Also, there are pressure taps at the 3% and 50% spans to ensure flow uniformity around the airfoil [18].

A stereo particle image velocimetry system (SPIV) is also used to measure three velocity components in the junction symmetry plane at up to 2 kHz sample rates. The dual-head Photonics laser source outputs light at a wavelength of 527 nm with maximum repetition rate of 10 kHz per head, and a maximum output pulse energy of 20 mJ per head. The SPIV system includes two Photron FASTCAM Mini UX100 high speed cameras with resolution of 1280×1024 pixels at 4 kHz. The captured images are processed using DaVis 8 software, and further processed using an in-house Matlab code. A detailed description of the wing pressure distribution validation and flow measurement design can be found in an earlier publication [18]. A hotwire probe has been used to obtain inlet turbulence intensity and length scales. Detailed information on the PIV and hotwire measurement techniques can be found in a parallel publication from the same laboratory [19].

B. Turbulence Grid

Figure 2 shows parallel PVC pipes, each with a diameter of 11.43 cm, which also equals the spacing between them. This design is based on the results of Roach [20]. The turbulence intensity (Tu) generated from this grid depends on the pipe diameter, spacing between the pipes, and distance from the grid to where turbulence intensity is measured. Using a hotwire probe, the turbulence intensity and the length scale are measured at $X/T = 5.10$ upstream of the Rood wing and at $Y/T = 3.00$ from the endwall. In this paper, unsteady surface heat flux measurements are also taken with and without turbulence grid to investigate the effects of added freestream turbulence levels on endwall heat transfer on the symmetry plane and around the wing body.

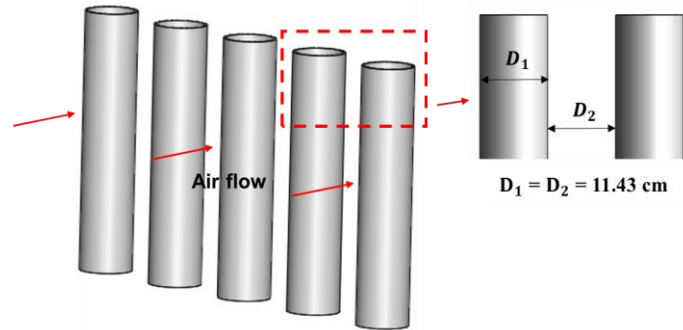


Figure 2. A parallel array of round PVC pipes is used as a turbulence grid

C. Test Conditions

Figure 3 shows a cross-sectional view of a constant surface temperature boundary condition in front of Rood wing achieved by applying constant heat flux (q'') on the underside of a 3.81 cm thick aluminum plate. To ensure the homogeneity of surface temperature, aluminum 6061 with a thermal conductivity of 167 W/m-K has been chosen. A conjugate CFD analysis has been performed to ensure that the aluminum would represent a constant surface temperature boundary condition around the junction. Also, surface thermocouples and an infrared camera have been employed to monitor the constant temperature of the surface during data collection. The heaters that provide constant heat flux both upstream as well as to the underside of the aluminum plate are made out of specially designed serpentine Inconel circuit encapsulated in Kapton. To increase the uniformity of surface heat flux, a very thin layer of copper is placed on top of the encapsulated Inconel circuit. Insulating foams with very low thermal conductivity are used to limit the conduction losses from the heaters. A CFD model of the mixed boundary

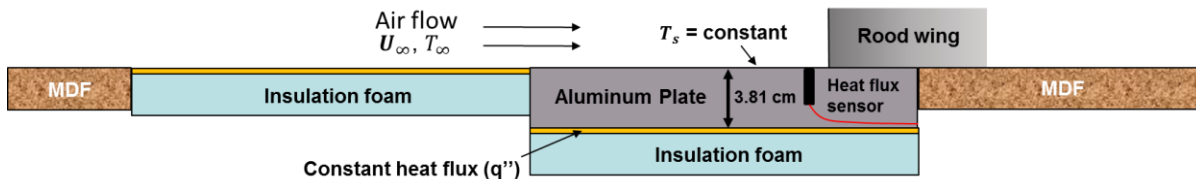


Figure 3. Time-resolved surface heat transfer measurements are taken by applying constant surface temperature boundary condition.

conditions shown in Figure 3 (constant heat flux upstream, constant surface temperature downstream) showed negligible change to the turbulent thermal boundary layer, relative to a constant surface temperature condition over the entire thermal boundary layer development length. The temperature difference between the two heating types is maintained to less than 1.5° C at the joint of both boundary conditions. The wind tunnel freestream velocity is measured with a pitot probe at the mid-span of the test section and the freestream temperature (T_∞) is measured with thermocouples at 10%, 25% and 50% of the test section span.

Time-resolved endwall heat transfer measurements are reported in this paper using a thermopile-based heat flux sensor [21]. Heat flux is determined through a Vatec HFM-7E/L heat flux microsensors (HFM). The sensor has a 6.32mm diameter face that measures surface temperature through a resistance temperature sensing element (RTS) on the outer edge of the cylindrical sensor, and heat flux (HFS) through a thin-film thermopile on face of the sensor. Both mechanisms output respective voltages that can be converted to surface temperature and heat flux using calibration constants from the manufacturer [21]. The RTS and HFS signals are amplified using a low-noise amplifier provided by Vatec Corporation before they are sent to a DAQ system [22]. The HFM sensor has a thin highly emissive black coating on its surface as well as a rise time of 900 μ s from 0 to 95% [22]. The sampling of unsteady heat transfer is conducted with a sampling rate of 5 kHz and the data is taken for 30s. Two HFM sensors and amplifiers are used in this study to examine how leading edge vortices interact with downstream secondary vortices. A process has been implemented using a standardized reference gauge by the manufacturer to calibrate both sensors and amplifier simultaneously [21].

The operational procedure for the sensors is as follows: before turning on the wind tunnel, RTS and HFS signals from HFM sensors are zeroed at room temperature with no heat flux applied. The desired Reynolds number is then achieved in the wind tunnel by changing the fan speed and power is supplied to both upstream heaters as well as to the heaters on the underside of the aluminum plate. The aluminum plates reach a steady temperature in about three hours. The voltage data is collected from the HFM sensors when it is determined that aluminum plates have reached a steady temperature condition. This process of getting to steady plate temperature is repeated everytime tunnel fan speed is changed to obtain a different Reynolds number.

An in-house post-processing routine is implemented to convert the instantaneous voltages to heat flux measurements using the guidelines provided from the HFM sensor manufacturer ([21],[22]). At first, the instantaneous RTS voltage ($V_{RTS}(t)$) from the DAQ system is low-pass filtered with a cutoff frequency of 2 kHz using a 20th order filter. This low pass filtered voltage is then used to calculate instantaneous resistance as shown in Eq. (1). Here, I_{RTS} and G_{RTS} are the excitation current and amplifier gain respectively. R_a is the ambient sensor resistance at ambient temperature. In Eq. (2), the HFM temperature $T(t)$ is found using instantaneous resistance ($R(t)$) and the RTS linearity and zero constants such as c and d , which are obtained from the calibration sheet provided by the manufacturer [21].

$$R(t) = \frac{V_{RTS}(t)}{(I_{RTS}) * (G_{RTS})} + R_a \quad \text{Eq. (1)}$$

$$T(t) = c * R(t) + d \quad \text{Eq. (2)}$$

The instantaneous heat flux is then found from the instantaneous voltage signals from HFS and sensor temperature $T(t)$ as shown in Eq. (3). In Eq. (3), G_{HFS} is the amplifier gain for HFS channel and g and h are calibration coefficients provided by the manufacturer [21].

$$q''(t) = \frac{V_{HFS}(t) / G_{HFS}}{g * T(t) + h} \quad \text{Eq. (3)}$$

The heat flux signals from HFM sensors have been corrected for radiation losses using an emissivity constant of 0.95. Radiation losses account for 26% to 7% of the total heat flux measured by the sensor as the freestream velocity is increased in the tunnel. Conduction losses are deemed negligible because the heat flux sensor is fully embedded in the large aluminum plate, and the sides of plates are well-insulated during data collection. The contribution from natural convection is not accounted for in the heat flux measurements as an analysis indicates negligible effects for the test conditions studied.

In this study, the HFM sensors are installed in five designated areas as shown in Figure 4. Two HFM sensors are used for simultaneous measurements. Both sensors are independently validated against a two-dimensional turbulent boundary layer correlation at the far upstream location 1, which is unaffected by the horseshoe vortex. The sensors remain completely flush with the surrounding aluminum surfaces ensuring no obstruction in the flowfield. The sensors are fully embedded and in thermal equilibrium with the large aluminum plate which results in negligible

impact to the thermal boundary layer. Also, the sensors are press-fitted into their positions which ensures minimum flow leakage. To capture the influence of the unsteady horseshoe vortex on the unsteady surface heat transfer in front of the leading edge, instantaneous voltage signals from HFM sensors have been acquired from location 2 and 3 concurrently. Furthermore, to understand how horseshoe vortex after being generated in front of the leading edge interacts with the downstream secondary vortices, instantaneous voltage signals are also taken from location 3 and 4 concurrently. Similar instantaneous voltage signals from HFM sensors are also taken from location 3 and 5.

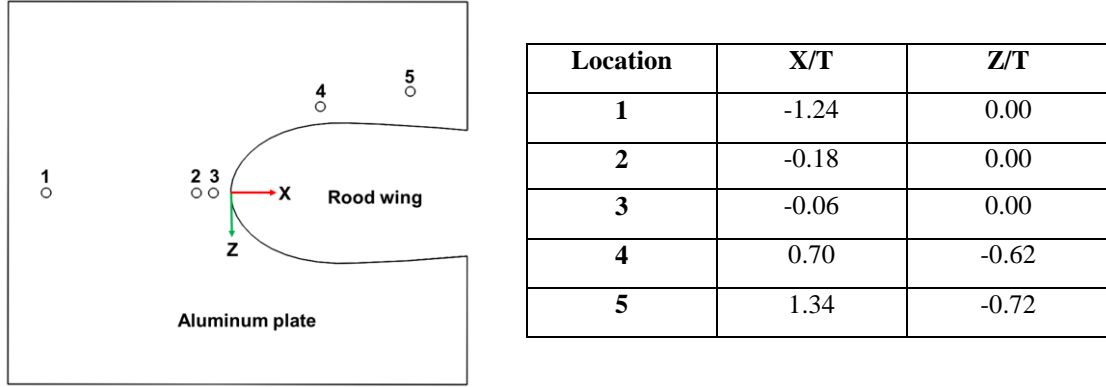


Figure 4. HFM sensor locations are shown both in front of and around the Rood wing. X and Z coordinates are non-dimensionalized by maximum body thickness of the Rood wing, $T = 9.42$ cm

D. Approach Boundary Layer and Heat Transfer Parameters

Unsteady surface heat transfer measurements are taken at a baseline freestream turbulence level as well as at a high freestream turbulence level representative of turbomachinery applications [15]. For each turbulence level, the tunnel flow speeds have been varied to obtain different Reynolds numbers based on Rood wing maximum thickness (T) as illustrated in Table 1. Table 1 also indicates inlet boundary layer conditions as well as surface and freestream temperatures for each Reynolds number case.

Table 1. Summary of experimental cases

Parameters	Low Tu			High Tu		
Tu %	1.0	1.1	1.1	21	17.7	15.2
T (cm)	9.42	9.42	9.42	9.42	9.42	9.42
U_{ref} (m/s)	1.16	4.19	13.40	1.16	4.19	13.40
$Re_T = U_{ref}T/\nu$	7,000	25,000	80,000	7,000	25,000	80,000
$Re_\theta = U_{ref}\theta/\nu$	452	1279	2853	245	758	1473
δ/T	0.50	0.39	0.35	0.51	0.34	0.32
δ^*/T	0.091	0.075	0.051	0.061	0.041	0.028
θ/T	0.061	0.053	0.038	0.039	0.030	0.020
l (m)	0.177	0.218	0.362	0.089	0.061	0.069
T_s (K)	311.7	312.3	309.7	310.0	310.0	308.6
T_∞ (K)	286.3	287.3	290.2	286.5	286.4	290.0

IV. Measurement Validation and Uncertainty Analysis

To validate the sensor measurements, time-averaged Stanton number is captured from sensor location 1 and plotted in Figure 5(a). Figure 5(a) also shows two-dimensional turbulent flat plate boundary layer correlation results and results from a previous study [18] conducted in the same wind tunnel at body thickness Reynolds number of 25,000 and 50,000. That study used a constant heat flux boundary condition over the entire endwall surface, where spatially resolved but time-average heat transfer coefficients were determined by measuring the surface temperature of the heater with an infrared camera. Only baseline freestream turbulence (1.0%) is provided in this figure to validate the results against the turbulent flat plate boundary layer correlation and the previous study [18]. As seen in Figure 5(a), time-averaged Stanton number decreases with increasing body thickness Reynolds number for the current study as well as for turbulent flat plate boundary layer correlation and Elahi et al. [18] case as expected. Also evident in Figure 5(a), the time-averaged Stanton numbers from the current study agree well with the turbulent

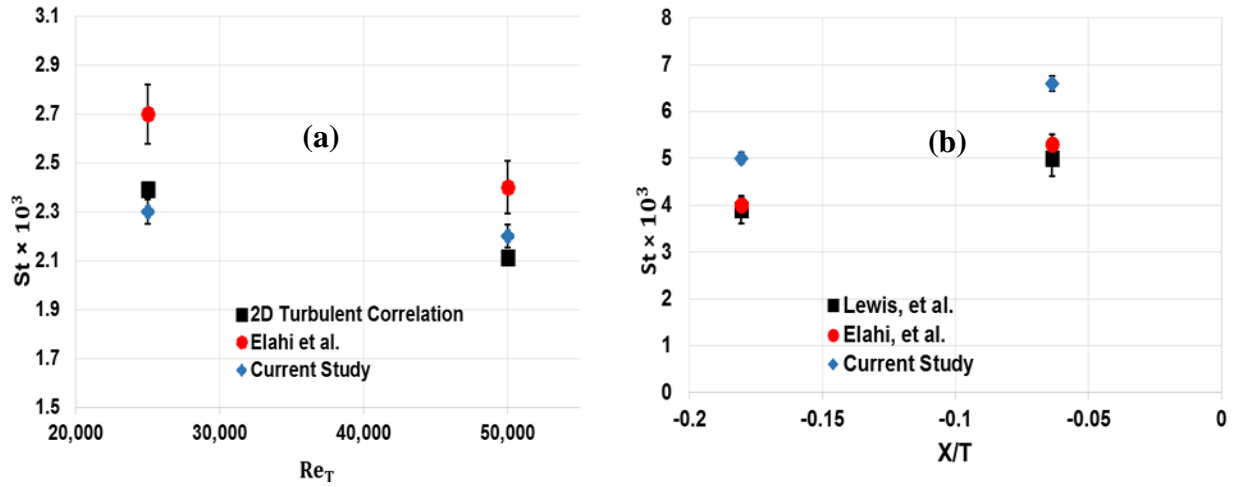


Figure 5. (a) Time-averaged Stanton numbers from current study are compared with 2D turbulent correlation and Elahi et al. [18] at Reynolds number of 25,000 and 50,000 and (b) time-averaged Stanton number from sensor locations 2 and 3 are plotted with findings from Lewis et al. [4] and Elahi et al.[18]

correlation at both Reynolds number cases. In Figure 5(b), time-averaged Stanton numbers from sensor location 2 and 3 are compared with the time-averaged Stanton numbers from the same upstream locations in Lewis et al. [4] and Elahi et al [18]. Additionally, the X distance is non-dimensionalized by the maximum wing thickness (T). Here, the time-averaged Stanton numbers from the current study is found to be 20% higher at $X/T = -0.18$ and 22% higher at $X/T = -0.06$ than the previous studies. Lewis et al.[4] reported an uncertainty of 15. 2% in the HFM measurements. Elahi et al. [18] reported an uncertainty of 8% in the Stanton number measurements of their highest Reynolds number case.

The overall uncertainty in time-averaged Stanton number (St_{mean}) and root mean square of instantaneous Stanton number (St_{RMS}) are found by taking seven sample datasets from location 2 as shown in Figure 4. For each dataset, an in-house Matlab routine calculates the mean and RMS of Stanton number from 150,000 data points (30 seconds at 5 kHz). The bias uncertainty of the HFM is 3.0% as provided by the manufacturer [21]. The precision uncertainty has been calculated using the standard 95% confidence interval. Table 2 shows the percent overall uncertainty in time-averaged and RMS of Stanton number for two extreme Reynolds number cases. The uncertainties are dominated by uncertainty in the sensor calibration as well as by the variations in freestream temperature and surface temperature.

Table 2. Summary of experimental uncertainties

Turbulence Level	Low Tu		High Tu	
Re_T	7,000	80,000	7,000	80,000
% uncertainty in St_{Mean}	4.00	4.80	3.75	3.50
% uncertainty in St_{RMS}	3.90	4.10	4.20	3.30

V. Results and Discussion

A. Comparison Between Symmetry Plane Sensor Locations

To show the respective locations of sensor 2 and 3 on the endwall in front of the wing leading edge, Figure 6 highlights the sensor locations in time-averaged normalized streamwise velocity magnitude contour plots for Re_T of 7,000 and 80,000 [19]. The time-averaged vortex core is shown to be in between the two sensors in both flowfields. In an instantaneous flowfield not shown in Figure 6, the vortex core is found to be extremely dynamic and unsteady over the sensor locations as Reynolds number increases. Also, Figure 6 shows a spatially and time-resolved endwall heat transfer contour plots [18] in terms of local Stanton number along with respective sensor locations with white circles. More details on measurement techniques and results of spatially and time-resolved endwall heat transfer can be found in Elahi et al. [18].

Unsteady heat transfer measurements are taken from sensor locations 2 and 3 (shown in Figure 4 & 6). Locations 2 and 3 are on the plane of symmetry and within the turbulent junction flow dominated region [18]. Two HFM sensors are employed to capture time synchronized data at a sampling rate of 5 kHz over the duration of 30 seconds per collection. Three trials are taken from locations 2 and 3 for a given Reynolds number and turbulence level.

As shown in Figure 7, time-averaged Stanton number and RMS in Stanton number are displayed at baseline and high freestream turbulence cases. In Figure 7(a), time-average St decreases with increasing Re_T (also Re_0 ; see Table 1) for a given turbulence level. This is not necessarily due to movement of the time-average vortex away from a sensor location; Figure 6 indicates that the time-average flowfield is similar despite the order of magnitude difference in Reynolds number, and the decrease is primarily due to the definition of St with the reference velocity in the denominator.

The effect of turbulence on the junction heat transfer appears to be a function of Reynolds number also. Focusing on location 2 in Figure 7(a), time-averaged Stanton number is shown to increase with increasing freestream turbulence at Re_T of 7,000 and 25,000. However, time-averaged Stanton number is shown to remain almost unchanged with increasing freestream turbulence at Re_T of 80,000. This conclusion of negligible change in time-averaged Stanton number as Re_T increases is in agreement with Ames et al. [17], who reported that the lack of influence of freestream turbulence on Stanton number at high Re_T is mainly due to a large inlet momentum thickness. Similar to location 2, location 3 also reports negligible augmentation in time-averaged Stanton number at Re_T of 80,000 as shown in Figure 7(a).

Figure 7(b) highlights the fluctuation in Stanton number at locations 2 and 3 with two freestream turbulence cases. Location 3, which is closer to the junction, experiences higher fluctuations in heat flux than location 2 at a respective turbulence level. It is also evident from Figure 7(b) that RMS in Stanton number is relatively large in low Re_T case as opposed to high Re_T case. In both sensor locations, the impact of added freestream turbulence on the RMS values is more significant at Re_T of 7,000 than at

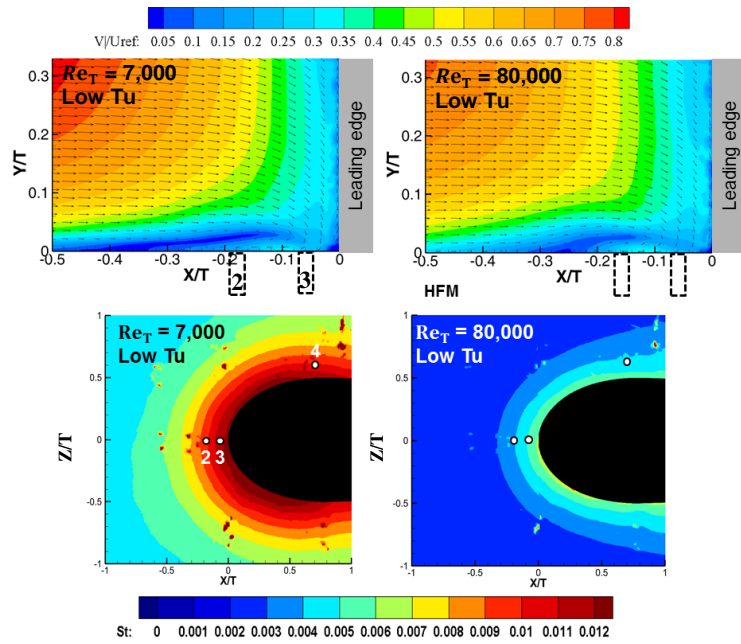


Figure 6. Sensor locations are shown in time-averaged flowfield and heat transfer measurements

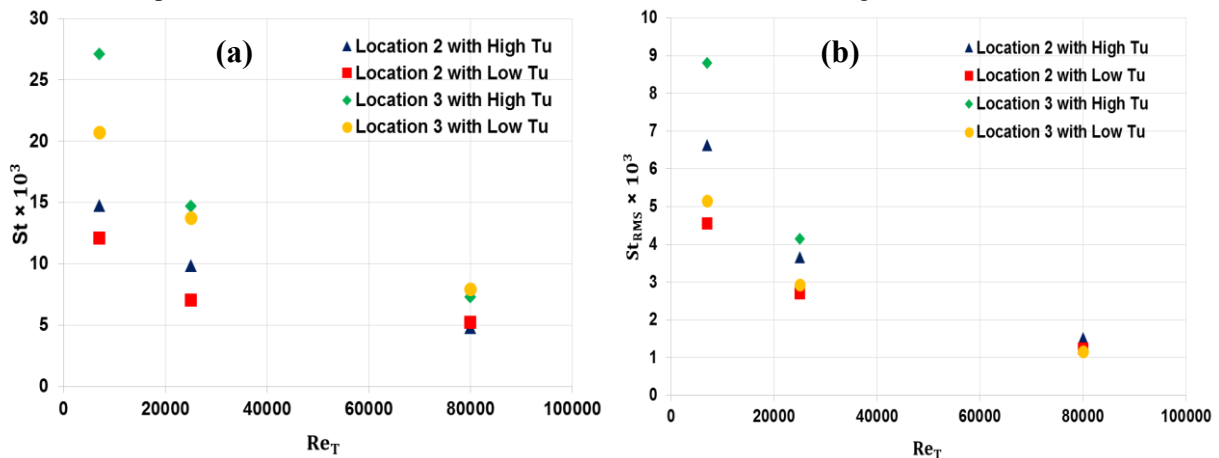


Figure 7. (a) Time-averaged Stanton number upstream of the wing on the symmetry plane, and (b) RMS in Stanton number from same upstream locations.

80,000. This is mainly due to the relative increase in the strength of heat flux fluctuations at low Re_T case with added turbulence.

The flowfield measured with the PIV system helps to explain the trend of turbulence level insensitivity in the St fluctuations at high Re . Figure 8 shows contour plots of the RMS of normalized u-velocity fluctuations obtained with the PIV system in the symmetry plane upstream of the wing, for the four cases investigated here. Overlaid vectors indicate the in-plane time-average velocity components, and the boxes below each subfigure indicate the heat flux sensor location. In general, the RMS of u-fluctuations is high underneath the time-average vortex core due to the aperiodic switching between the backflow and zero-flow modes of the vortex, which contributes to high RMS of St . When comparing between low and high Reynolds number cases at low turbulence level in Figure 8, the levels of normalized u-velocity fluctuations near the sensor locations are generally similar, which would imply similar heat flux fluctuation levels. Note that in Figure 7(b), the RMS of St decreases with Re_T since the denominator of St (and St_{RMS}) includes the reference velocity, which is increasing with Re_T .

The more interesting comparison in Figure 8 is the difference in u-velocity fluctuations between low and high turbulence levels, for a given Reynolds number. For the low Re_T , there is a distinct increase in u-velocity fluctuations in the time-average vortex core region and the heat flux sensor locations. This is due to the sensitivity of the horseshoe vortex to the freestream turbulence. However, at high Re_T , the fluctuation levels in the vortex core region and near the endwall are not significantly affected by high freestream turbulence, which agrees with the trend of the heat flux fluctuations in Figure 7(b).

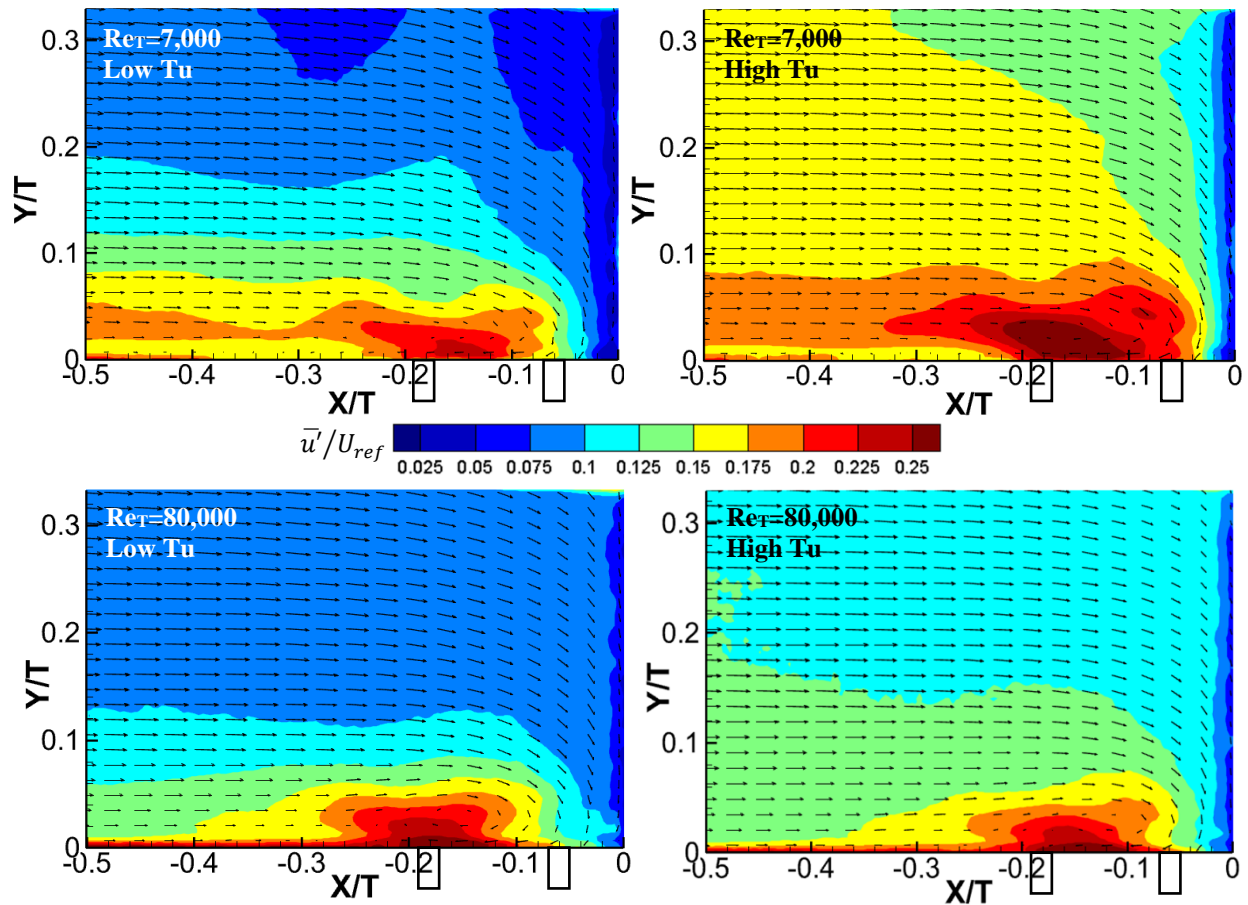


Figure 8. Contours of normalized u-velocity fluctuations, overlaid with time-average velocity vectors, and heat flux sensor locations given in the boxes.

The PDFs shown in Figure 9 are of the heat flux fluctuations for locations 2 and 3. These PDFs are normalized by subtracting the time-mean heat flux from the instantaneous heat flux signals and then dividing the outcome by the RMS of the same instantaneous heat flux signals [4]. PDFs of heat flux fluctuations in the turbulent horseshoe vortex dominated region (i.e. sensor locations 2 and 3) do not exhibit a bimodal nature, which is consistent with the findings by Lewis et al [4]. A bimodal structure is present in the PDFs of fluctuating streamwise velocity components reported

by Devenport and Simpson [3]. The effects of the unsteady behaviors in heat flux fluctuations are exhibited by the distortions of the PDF from a Gaussian PDF. The skewness (Sk) and kurtosis (Ku) of each PDF are also highlighted

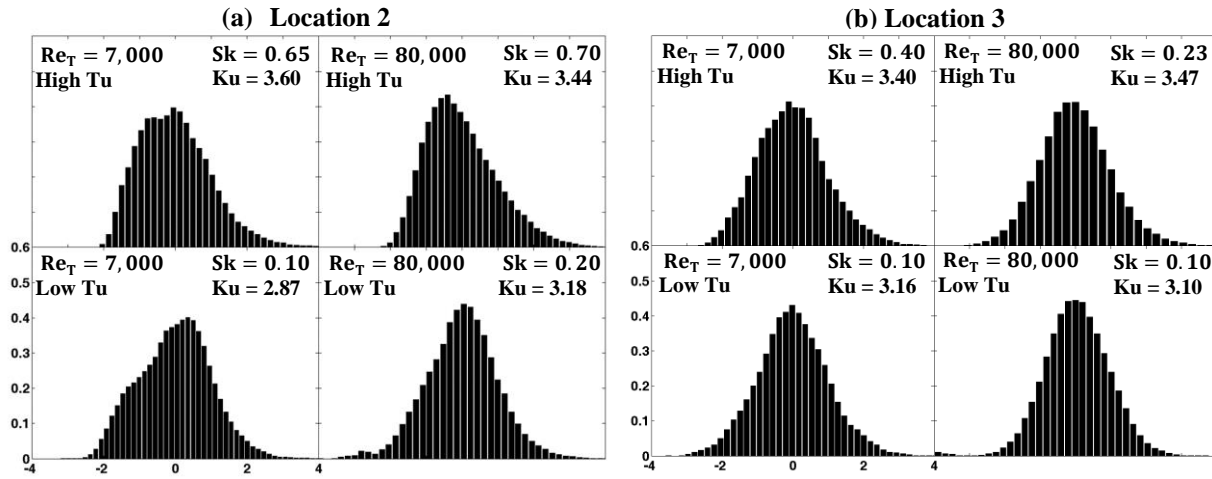


Figure 9. (a) PDFs of heat flux fluctuations at location 2 are shown for low and high Reynolds number and turbulence cases, (b) PDFs of heat flux fluctuations at location 3 are shown in the same fashion.

in Figure 9. For reference, a Gaussian distribution would have a Sk and Ku of 0 and 3 respectively. For high turbulence in both sensor locations, the Sk values are more positive than the low turbulence case suggesting that there is an increased number of positive-value fluctuations events with freestream turbulence, especially for low Re_T . Ku levels are also higher for the high turbulence cases, suggesting a broader distribution of heat flux events.

B. Comparison between Leading Edge and Side of Wing

To understand how the unsteady horseshoe vortex upstream of the leading edge interacts with the secondary vortices downstream of the leading edge and influences the endwall heat transfer, time synchronized heat flux measurements are captured from locations 3 and 4 at a sampling rate of 5 kHz over the duration of 30 seconds. In Figure 10(a), at the baseline turbulence as well as at the high turbulence level, time-averaged Stanton number drops significantly between locations 3 and 4 at Re_T of 7,000. The higher values of time-averaged Stanton number at the location 3 are mainly caused by the swirling motion in the horseshoe vortices. However, as the Re_T approaches 80,000, the influence of added freestream turbulence becomes negligible in sensor locations 3 and 4 validating the findings by Ames et al [17]. Furthermore, the effect of increased turbulence on time-averaged Stanton number in location 4 is shown to be insignificant in all Re_T cases. This suggests that freestream turbulence may have more

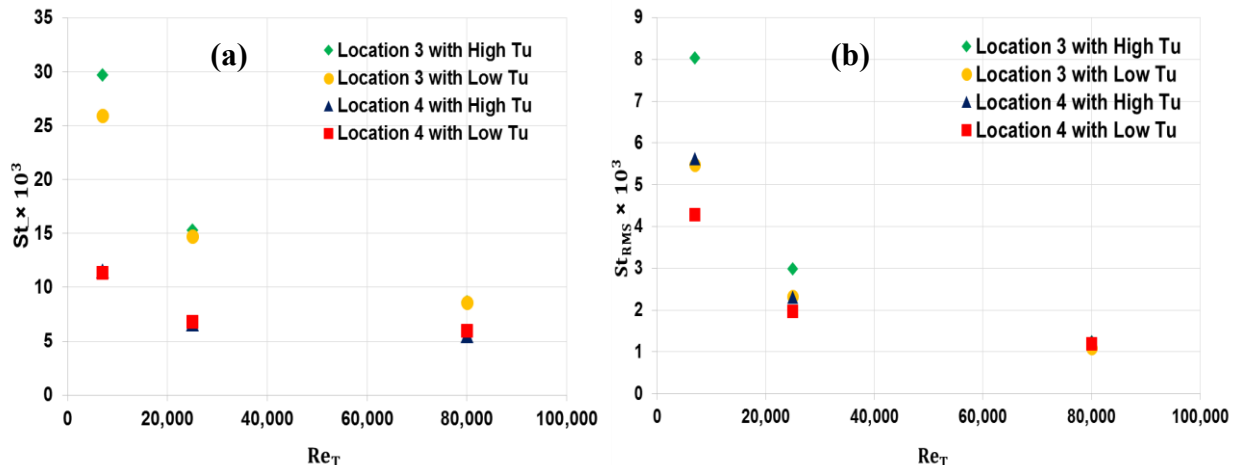


Figure 10. (a) Time-averaged Stanton number is compared between leading edge and side of the wing , and (b) RMS in Stanton number is reported from the same locations.

impact on the horseshoe vortex dominated region at the plane of symmetry than in the downstream secondary vortex dominated region (location 4). Figure 10(b) highlights the RMS in the Stanton number at locations 3 and 4. RMS values in locations 3 and 4 are relatively high when Re_T is 7,000 for both turbulence levels. When Re_T equals 80,000, RMS values are shown to become relatively low. Also, it is noted that RMS values change dramatically with added freestream turbulence at lower Re_T than they do at higher Re_T .

The PDFs shown in Figure 11 are of the heat flux fluctuations for locations 4 and 5. Note that locations 4 and 5 are both downstream from the wing leading edge. These PDFs are normalized in the same way as Figure 9. The double-peaked or bimodal structures are also absent in PDFs at locations 4 and 5. This absence of bimodal structures is expected in locations 4 and 5 where the leg of the horseshoe vortex, and a mild skewed turbulent flat plate boundary layer (due to the wing pressure field) tend to dominate, respectively. The Figure 11 also includes Sk and Ku for each PDF. Sk and Ku both increase with turbulence level for Re_T of 7,000. Also, for Re_T of 80,000 at low Tu, Sk and Ku follow a Gaussian distribution, and are increased with increasing Tu due to an increase in positive-magnitude fluctuation events.

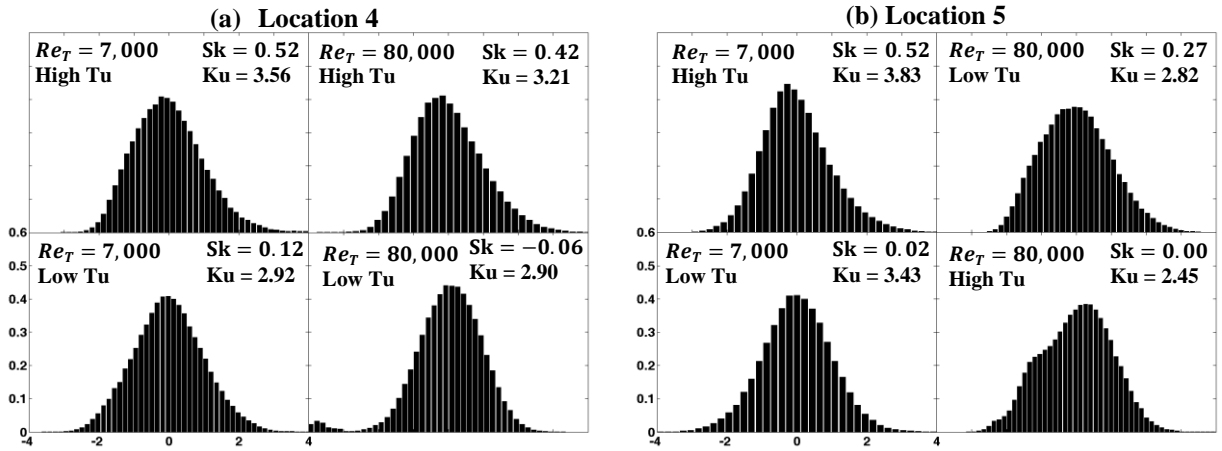


Figure 11. (a) PDFs of heat flux fluctuations at location 4 are shown for low and high Reynolds number and turbulence cases, (b) PDFs of heat flux fluctuations at location 5 are also shown in the same fashion.

C. Comparison between Leading Edge and Far Downstream

To further the understanding in the interaction between the unsteady horseshoe vortex and downstream secondary vortices, in Figure 12, time-averaged Stanton number from location 5 (which is even further downstream from the leading edge) is compared with the Stanton number at location 3 where horseshoe vortex dominates. Figure 12(a) shows sensor location 5 is not much affected by either the increased freestream turbulence or by the increased Reynolds number. This behavior may suggest that location 5 is in a 2D turbulent boundary layer region where

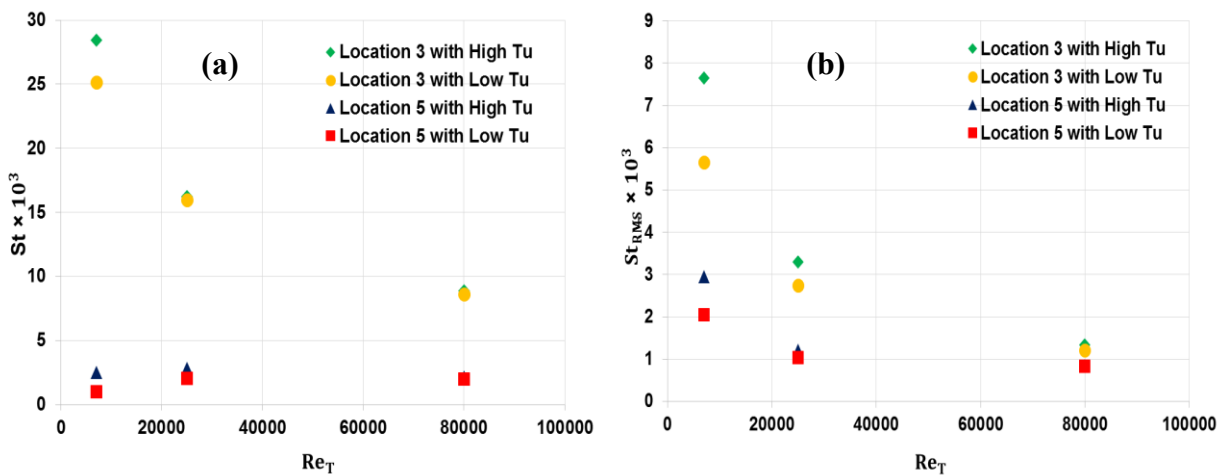


Figure 12. (a) Time-averaged Stanton number is compared between leading edge and further downstream of the wing, and (b) RMS in Stanton number is reported from the same locations.

neither the secondary vortices nor the swirling motion from the symmetry plane played any role to influence endwall heat transfer. Figure 12(b) shows the RMS in Stanton number at locations 3 and 5. Just like the RMS values in locations 3 and 4, RMS values in locations 3 and 5 are higher at the low Reynolds number cases for both turbulence levels. When Re_T equals 80,000, RMS values are shown to become considerably low.

D. Augmentation in Stanton Number

Time-averaged Stanton number for high turbulence case is divided by the time-averaged Stanton number for baseline turbulence case to calculate the net augmentation in Stanton number due to turbulence. Figure 13 illustrates a summary of augmentation in Stanton number at all four sensor locations at three Reynolds number cases. Locations 2 and 3 are located in the horseshoe vortex dominated region [18]. The Stanton number augmentation in this horseshoe vortex region varies from 1.20 to about 1.00 as Reynolds number is increased from 7,000 to 80,000. This shows that at high Reynolds number case, freestream turbulence does not influence the endwall the heat transfer, which is one of the conclusions drawn by Ames et al [17]. The augmentation in Stanton number in horseshoe vortex dominated region (locations 2 and 3) at Reynolds number of 25,000 is further validated by comparing to Radomsky and Thole [15], who reported an augmentation of 1.15 within the horseshoe dominated region of the leading edge of a vane at a similar

approach Reynolds number. Sensor location 4 is placed relatively closer to the wing body compared to location 5, which is further downstream and away from the wing body. The augmentation in Stanton number in location 4 tends to stay around 1.00 as the Reynolds number is increased as shown in Figure 13. This behavior apparently shows that freestream turbulence played little role in increasing endwall heat transfer at location 4. However, at location 5 freestream turbulence contributes to increase endwall heat transfer by a factor of 2.50 at Re_T of 7,000.

E. Power Spectra Analysis

The normalized power spectrum density (PSD) in Figure 14 demonstrates the frequency content of the unsteady Stanton number both on symmetry plane and around the airfoil. The frequency is normalized by T/U_{ref} on the x-axis and on the y-axis, power spectrum density G , is normalized by U_{ref}/T and the square of the time-averaged Stanton number. This normalization technique allows for the area under the PSD curve to be representative of the variation in Stanton number. Three different Reynolds numbers are used as shown in Figure 14. Also, in Figure 14, comparisons are made between high and low Tu intensities at four sensor locations. The results in Figure 14 are not corrected for the finite size of the HFM sensors and the PSD curves at very high frequencies may have been attenuated [4].

In Figure 14, PSD curves for locations 2 and 3 in both low and high turbulence cases have a slight downward slope at low frequency spectral levels followed by a rolloff as the frequency increases. The PSD for Re_T of 7,000 is shown to plateau at high frequencies due to possible attenuation in both locations 2 and 3. The rolloff slopes for Re_T of 25,000 and 80,000 seem to match at low and high turbulence cases. In low frequency region, the spectral density amplitudes are larger at Re_T of 7,000 and 25,000 than 80,000, which is found to be consistent for both low and high turbulence cases. This increase in amplitude at lower Reynolds numbers is contributed by the high levels of heat flux fluctuations also evident in the RMS values in Figure 7(b). At low turbulence case, the spectral density amplitudes seem to decrease slightly at all three Reynolds numbers compared to high turbulence case also evident in the RMS values in Figure 7(b). Figure 14 also shows the spectral density amplitudes for sensor locations 4 and 5, which are from the downstream region, appear to be a little low for location 4 and much lower for location 5 when compared

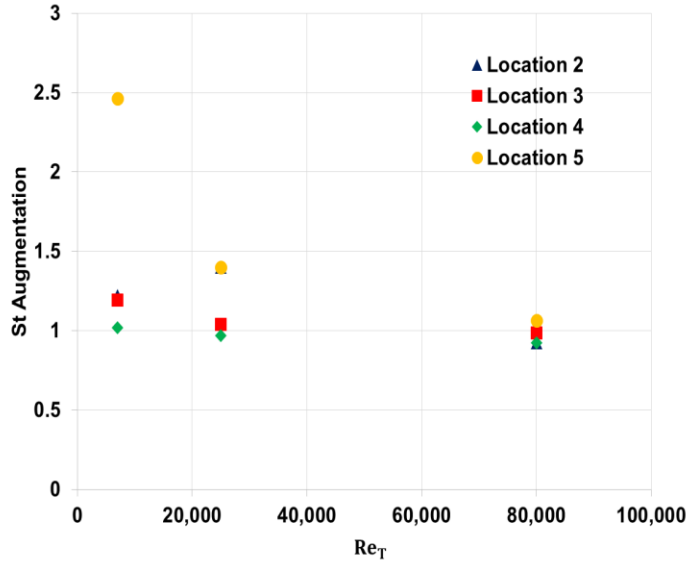


Figure 13. Augmentation in Stanton number due to turbulence

with the amplitudes for locations 2 and 3. This is again consistent with the heat flux fluctuations found in locations 4 and 5 from the Figure 10(b) and Figure 12(b).

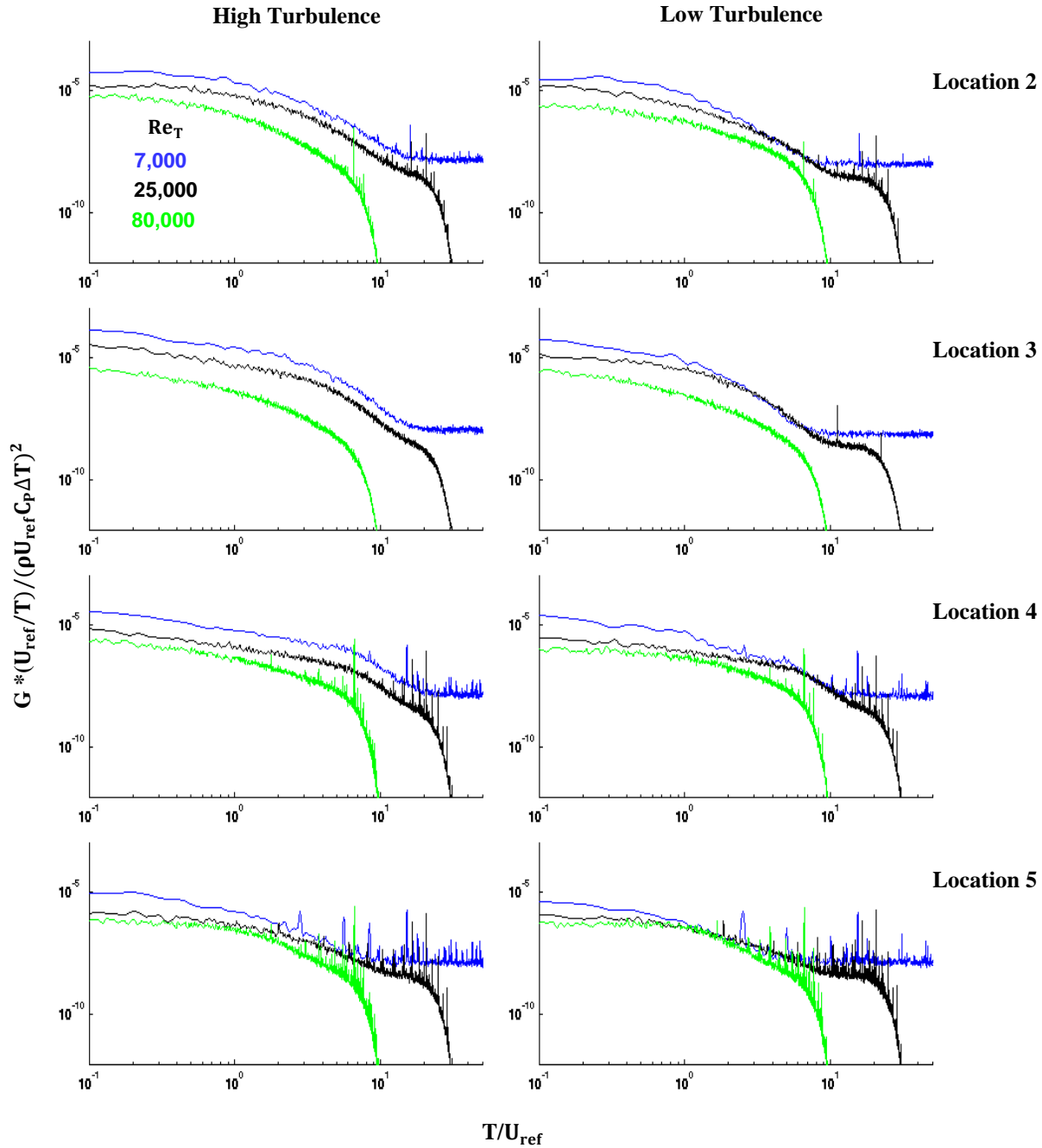


Figure 14. Normalized power spectrum density curves show heat flux fluctuations are higher on the plane of symmetry at the high turbulence level.

VI. Conclusions

A recirculating low-speed wind tunnel is used to understand the effects of high freestream turbulence and various Reynolds numbers on turbulent junction flowfield and endwall heat transfer. Time-resolved heat flux measurements from turbulent junction endwall as well as from the downstream of the Rood wing leading edge are

presented in this paper. Statistical analyses on the normalized heat flux fluctuations are also shown for all four sensor locations. A thorough comparison of the one-sided autospectral density functions are presented for four sensor locations at all three Reynolds numbers to highlight the variance of the local Stanton number. Following are some specific conclusions:

- (a) At lower Reynolds numbers (i.e. 7,000 and 25,000), time-averaged endwall Stanton number in the turbulent junction flow region is shown to increase dramatically with added freestream turbulence. At high Reynolds number (i.e. 80,000), the change in endwall Stanton number near the junction becomes negligible with increasing turbulence, which agrees with the prior work by Ames et al. [17].
- (b) In the turbulent junction flow dominated region, the fluctuations in heat flux increase as the junction is approached from upstream, and it is found to be true at low and high turbulence levels. The PDFs of heat flux fluctuations near the junction (i.e. sensor locations 2 and 3) do not exhibit a bimodal distribution, which is consistent with prior work in this field [4].
- (c) The endwall Stanton number augmentation due to turbulence in the junction flow region varies from 1.20 to about 1.00 as Reynolds number is increased. Insignificant augmentation in Stanton number in sensor location 4 (which is located around the wing body) shows freestream turbulence played a little role in increasing endwall heat transfer.
- (d) Power spectrum density (PSD) amplitudes are found to be larger at lower Reynolds number cases than the high Reynolds number case showing that high levels of heat flux fluctuations are present at lower Reynolds number cases. Also, amplitudes are shown to decrease at the low turbulence case for all four sensor locations meaning with decreasing freestream turbulence, the fluctuations also decrease near the junction and around the wing body.

VII. Acknowledgements

This work was sponsored by the Office of Naval Research, ONR, under grant number N00014-15-1-2764; the views and conclusions contained herein are those of the authors and should not be interpreted as necessarily representing the official policies or endorsements, either expressed or implied, of the Office of Naval Research, the U.S. Navy or the U.S. government.

VIII. References

- [1] Praisner, T. and Smith, C., 2006, "The Dynamics of the Horseshoe Vortex and Associated Endwall Heat Transfer—Part I: Temporal Behavior," *Journal of Turbomachinery*. 128(4), pp. 747-754.
- [2] Han, J.-C., Dutta, S., and Ekkad, S., *Gas turbine heat transfer and cooling technology*. 2012: CRC Press.
- [3] Devenport, W.J. and Simpson, R.L., 1990, "Time-depeiident and time-averaged turbulence structure near the nose of a wing-body junction," *Journal of Fluid Mechanics*. 210, pp. 23-55.
- [4] Lewis, D., Simpson, R., and Diller, T., 1994, "Time-resolved surface heat flux measurements in the wing/body junction vortex," *Journal of thermophysics and heat transfer*. 8(4), pp. 656-663.
- [5] Simpson, R.L., 2001, "Junction flows," *Annual Review of Fluid Mechanics*. 33(1), pp. 415-443.
- [6] Anderson, C.D. and Lynch, S.P., 2016, "Time-resolved stereo PIV measurements of the horseshoe vortex system at multiple locations in a low-aspect-ratio pin–fin array," *Experiments in Fluids*. 57(1), pp. 5.
- [7] Paik, J., Escarriaza, C., and Sotiropoulos, F., 2007, "On the bimodal dynamics of the turbulent horseshoe vortex system in a wing-body junction," *Physics of Fluids*. 19(4), pp. 045107.
- [8] Yakhot, A., et al., 2006, "Direct numerical simulation of turbulent flow around a wall-mounted cube: spatio-temporal evolution of large-scale vortices," *Journal of Fluid Mechanics*. 566(1), pp. 1-9.
- [9] Apsilidis, N., et al., 2015, "Time-resolved flow dynamics and Reynolds number effects at a wall–cylinder junction," *Journal of Fluid Mechanics*. 776, pp. 475-511.
- [10] Chen, Q., et al., 2017, "Experimental study on the multimodal dynamics of the turbulent horseshoe vortex system around a circular cylinder," *Physics of Fluids*. 29(1), pp. 015106.
- [11] Hada, S., et al., 2008, "The effect of leading edge diameter on the horse shoe vortex and endwall heat transfer," *ASME Turbo Expo 2008: Power for Land, Sea, and Air*. pp. 813-823.
- [12] Blair, M.F., 1974, "An Experimental Study of Heat Transfer and Film Cooling on Large-Scale Turbine Endwalls," *Journal of Heat Transfer*, 96(4), pp.524-529.

- [13] Dunn, M. and Stoddard, F., 1979, "Measurement of Heat-Transfer Rate to a Gas Turbine Stator," *Journal of Engineering for Power*. 101(2), pp. 275-280.
- [14] Swisher, S., Diller, T., and Pierce, F., 1993, "Time-resolved heat flux measurements in a turbulent junction vortex," *ASME Publications-HTD*. 206, pp. 55-55.
- [15] Radomsky, R.W. and Thole, K.A., 2000, "Flowfield measurements for a highly turbulent flow in a stator vane passage," *Journal of Turbomachinery*, 122(2).
- [16] Kang, M.B., Kohli, A., and Thole, K., 1999, "Heat transfer and flowfield measurements in the leading edge region of a stator vane endwall," *ASME J. Turbomach.* 121(3), pp. 558-568.
- [17] Ames, F.E., Barbot, P.A. and Wang, C., 2003, "Effects of Aeroderivative Combustor Turbulence on Endwall Heat Transfer Distributions Acquired in a Linear Vane Cascade". *Journal of Turbomachinery*, 125(2), pp.210-220.
- [18] Elahi, S.S., Lange, E.A., and Lynch, S.P., 2017, "Experimental Measurements of Turbulent Junction Flow Using High Speed Stereo PIV and IR Thermography," *47th AIAA Fluid Dynamics Conference*. pp. 3303.
- [19] Lange, E.A., Elahi, S.S., and Lynch, S.P., "Time-resolved PIV Measurements of the Effect of Freestream Turbulence on Horseshoe Vortex Dynamics" in *Scitech 2018*. Penn State University University Park.
- [20] Roach, P., 1987, "The generation of nearly isotropic turbulence by means of grids," *International Journal of Heat and Fluid Flow*. 8(2), pp. 82-92.
- [21] Vatel Corporation, ed. "*HFM-6, HFM-7, & HFM-8 Operator's Manual*,". 2015.
- [22] Siroka, S., Shallcross, M., and Lynch, S., 2016, "Unsteady Heat Transfer Around Low Aspect Ratio Cylinders in an Array," *ASME 2016 International Mechanical Engineering Congress and Exposition*. pp. V008T10A039-V008T10A039.